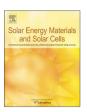
FISEVIER

Contents lists available at ScienceDirect

Solar Energy Materials & Solar Cells

journal homepage: www.elsevier.com/locate/solmat



Transient photocurrent and photovoltage mapping for characterisation of defects in organic photovoltaics



Sebastian Wood*, Daniel O'Connor, Christopher W. Jones, James D. Claverley, James C. Blakesley, Claudiu Giusca, Fernando A. Castro

National Physical Laboratory, Hampton Road, Teddington TW11 0LW, United Kingdom

ARTICLEINFO

Keywords: Printed solar cells Organic photovoltaics Defects Transient photovoltage Transient photocurrent Characterisation

ABSTRACT

Advances in organic photovoltaics have created the opportunity for low-cost, high-throughput manufacture of solar cells using roll-to-roll printing technology; however, the performance, reliability, and production yield of these devices can be critically limited by the incorporation of defects during fabrication. The detection and elimination of all printing defects is unrealistic, so techniques are required to identify those types of defects which are most critical to solar cell functionality. Here, we combine mapping of both surface topography and photovoltaic properties in order to understand the impact of various types of defect on the functional performance. To enable this comparison, transient photocurrent and photovoltage mapping is demonstrated as a technique for measuring local variation in charge carrier dynamics. We find that dust particle contamination corresponds with localised reductions in charge extraction rate. This novel measurement technique provides a way to distinguish between different types of defect by considering both the magnitude and dynamics of the local transient responses.

1. Introduction

It was recognised more than a decade ago that the economic viability of organic photovoltaic (OPV) technology is dependent upon the realisation of devices with a high power conversion efficiency (PCE), long operational lifetime, and low production cost [1]. Recent progress has led to PCEs above 11% for single junction organic solar cells, and there remains scope for further improvement [2,3]. These encouraging results have led to increased investment of resources into improving the operational lifetime and scaling up production of solar cells into a roll-to-roll printing process [4,5]. However, to produce high efficiency, stable OPVs on a large scale, it is important to mitigate the formation of defects, which can critically limit the device performance. OPV structures typically comprise multiple layers deposited in separate processes, and as a result, there are many different types of defect or inhomogeneity that may form. Some of these defects (e.g. shunt connections across the active layers) can be critical to the functionality of the device, whereas others are usually less serious (e.g. small variations in thickness of a metal electrode). It is, therefore, important to identify and quantify the critical defects for two reasons: to improve the manufacturing yield quickly by focusing on resolving the most critical problems, and to facilitate the implementation of in-line defect detection measurements based on machine learning and cataloguing

defect types [6]. In practice, this requires an understanding of the impact of specific types of defects on the functional performance of the solar cell. In this study, we develop a transient photocurrent and photovoltage mapping technique as a probe for local variation in the dynamics of photogenerated charge carriers. By combining this novel measurement with surface topography data and steady state photocurrent mapping, we are able to identify different types of defects and correlate them with their impact on photovoltaic performance. As an example, we consider the effects of particulate contamination, which is a typical problem for printing processes, by incorporating silica microspheres of known dimension into solution-deposited solar cells as reference 'dust' defects. In this case, we observe spatial variations in the transient photocurrent decay lifetime indicating a locally reduced charge extraction rate.

2. Methods

2.1. Sample preparation

Patterned indium tin oxide (ITO) substrates were first cleaned by ultrasonication in a series of acetone, Hellmanex detergent, deionised water, and isopropanol. Photovoltaic devices were then prepared in the inverted architecture: glass/ITO/ZnO/polymer:fullerene/MoO $_{x}$ /Ag.

E-mail address: sebastian.wood@npl.co.uk (S. Wood).

^{*} Corresponding author.

The ZnO layer was deposited by spin coating from a 160 g/l solution of zinc acetate (obtained from Sigma Aldrich) in dimethyl sulfoxide (DMSO) and immediately baked at 300 °C before rinsing with acetone and deionised water. Substrates were then dried at 140 °C for 10 min before transferring to a nitrogen-filled glovebox and baking for a further 10 min. The active layer comprised OPV100 (an electron-donating polymer) and the electron-accepting fullerene derivative (PC₆₁BM) both provided by Merck and dissolved in chlorobenzene with a ratio of 1:2 by weight, giving a 30 mg/ml solution. The solution was stirred for 2 h at 70 °C to ensure complete dissolution, and deposited on to the ZnO layer by blade coating to give an active layer thickness of 300 ± 20 nm. Samples were dried at 70 °C prior to deposition of the electrode by thermal evaporation of a 5 nm layer of MoO_x followed by 150 nm of Ag, at $<10^{-6}\,\mathrm{mbar}$ vacuum. The deposited electrodes defined device active areas of 1 cm².

In order to create the simulated 'dust' defects, silica microspheres were obtained from Whitehouse Scientific with a nominal diameter of 9 μm and dispersed in deionised water by ultrasonication with a concentration of roughly 10^6 microspheres/ml. For the samples incorporating the microspheres, the process described above was interrupted after the ZnO deposition and a droplet of the microsphere suspension was spin coated on to the centre of the sample at 4000 rpm for 10 s before drying at 80 °C for 10 min and then progressing to the active layer deposition.

2.2. Areal surface topography measurements

A Talysurf CCI HD Coherent Scanning Interferometer (CSI) manufactured by Taylor Hobson was used for areal surface topography measurements. A CSI extracts surface topography by first projecting broadband light onto the sample through an interferometric objective, in this case, of the Mirau type, and then mechanically scanning the sample through the interference contrast envelope that peaks at zero optical path difference. A series of areal images is recorded at regular displacements during the mechanical scan. An algorithm then processes the acquired interference fringe contrast and phase information to determine a surface height for each pixel in the image stack.

The CSI was fitted with a 10× magnification objective lens (0.3 numerical aperture, working field of view of 1.66 mm by 1.66 mm and sampling distance of approximately 0.8 µm) and used in stitching mode. The region size of the measured topography was 17.1 mm by 17.1 mm (slightly larger than the 16 mm by 16 mm sample), which was composed of 121 partially overlapped topographies in a measurement grid of 11 by 11. This raster and stitch measurement routine took approximately 4 h to complete. The vast majority (>90%) of this time was associated with the automatic lateral repositioning and focusing of the sample, and not the individual CSI measurements. The raster and stitch measurement was repeated after each of the various layer deposition steps during the fabrication of the OPV device and required the removal of the sample to a separate laboratory on site. This necessitated the development of a procedure to reposition the sample under the CSI instrument with good repeatability in order to enable registration of data from multiple layers with a high confidence. While every effort was made to protect the sample, the repeated and extended exposure to ambient conditions has contributed to the high density of defects observed in this study, in addition to the artificial defects.

Interferometric surface topography measurements can be affected by phase change errors on reflection due to inhomogeneities in material composition, which could result in errors of up to a few tens of nanometres. In this case, however, the subsequent layer depositions of uniform material compositions exhibited dimensional features that correlated with those in the previous layer, which is evidence that these features are in fact real dimensional defects propagating through the fabrication process and not simply artefacts of the optical measurement.

2.3. Laser beam induced current mapping

Laser beam induced current mapping was performed using a ReRa SpeQuest system customised with a Zaber x-y sample translation stage and modified optics to focus the 532 nm diode laser onto the sample. The spatial resolution was limited by the laser spot size (estimated to be 70–90 μm in diameter). A Thorlabs LCC3111 noise eater, positioned before the Thorlabs MC2000 mechanical chopper (270 Hz), was used to stabilise the laser output power (5 μW average incident on sample), and the photocurrent signal was amplified with a large dynamic range Melles Griot pre-amplifier and measured using a Stanford Research SR830 digital lock-in amplifier. An OSLON 80 9+ PowerStar LED array (peak emission at 617 nm) was used as a bias light, to control the opencircuit voltage of the device in order to approximate operational conditions during measurements.

2.4. Transient photovoltage mapping

Photovoltage & photocurrent transients were measured by connecting the sample device to a Tektronix DPO4104B oscilloscope (1 $M\Omega$ input impedance for transient photovoltage and $50\,\Omega$ for transient photocurrent) and exposing the sample to an excitation pulse from a Sirah PrecisionScan dye laser delivering pulses of duration < 10 ns, with wavelength 635 nm, a frequency of 10 Hz, and a pulse energy of 4 mJ. Spatial resolution was provided by focusing the excitation laser pulse to a spot approximately 50 μm in diameter, and translating the sample on a 2-axis stage to raster over the area of interest. Electrical noise generated by the 2-axis stage presents a significant problem, which is discussed further below.

The sample was contained within a nitrogen-filled sample chamber to prevent degradation, and no change in the transient response was observed on the time scales considered in this work. Transient responses were averaged over 64 measurements for each sample position.

3. Results and discussion

3.1. Surface topography mapping

After each layer deposition step of the device fabrication process (see Fig. 1(a)), the topography of the top surface of the sample was measured using coherence scanning interferometry, which is particularly suited to the measurement of these nominally planar samples [7]. This enables us to observe which new defects have been introduced at each stage, and to see how defects from previous steps have affected subsequent depositions. The resulting surface topography maps for each layer are shown in Fig. 1. Measurements were taken over the full 16 mm by 16 mm area of the sample, but a smaller 2.2 mm by 1.7 mm sub-region is considered here since we are interested in small features. The total thickness of the device (excluding the glass substrate) is around 700 nm and the diameter of the silica microspheres is an order of magnitude larger. As a result, the height-scales of the topography images measured after deposition of this 'dust' are truncated at 100 nm so that the smaller scale structure is clearly visible alongside the positions (but not heights) of the microspheres.

The surface topography maps in Fig. 1 show multiple features and defects that are present in the device, examples of which are labelled A-F in Fig. 1(c). The silica microspheres (e.g. 'A') are clearly visible as circular features in the $\mathrm{MoO_x/Ag}$ and active layer images but absent from the ZnO and ITO, as expected from the layer deposition sequence. The other defects, labelled 'B–F', were not introduced deliberately so their identities are unknown, however, by comparing the images of the different layers, we can identify at which point in the deposition process they first appear and can suggest likely causes. Defect 'B' is present in every layer (more clearly visible in the corresponding line profiles shown in the Supplementary information). Therefore, we

Download English Version:

https://daneshyari.com/en/article/6456995

Download Persian Version:

https://daneshyari.com/article/6456995

<u>Daneshyari.com</u>